Influence of transport coefficients on fission dynamics in the five-dimensional Langevin approach

K. Okada*
Advanced Science Research Center, Japan Atomic Energy Agency, Tokai, Ibaraki 319-1195, Japan

T. Wada
Department of Pure and Applied Physics, Kansai University, Suita, Osaka 564-8680, Japan

N. Carjan
Joint Institute for Nuclear Research, 141980 Dubna, Moscow Region, Russia
Centre d'Etudes Nucleaires de Bordeaux-Gradignan,
UMR 5797, CNRS/IN2P3-University Bordeaux I, BP 120, 33175 Gradignan Cedex, France
and Horia Hulubei - National Institute for Nuclear Physics and Engineering, P.O.Box MG-6, RO-76900, Bucharest, Romania

(Received 31 March 2025; accepted 1 August 2025; published 19 September 2025)

Transport coefficients in the Langevin equation are essential for the dynamical analysis of nuclear fission. Two primary methods for calculating these coefficients exist: macroscopic and microscopic. Here we study the fission of ^{236}U using a five-dimensional Langevin equation with a Cassini shape parametrization to examine how the choice of transport coefficients affects the distributions of fission fragment mass, quadrupole (β_2), octupole (β_3), and total kinetic energy. The results indicate that microscopic transport coefficients generate fragments with a broader range of deformation, which improves the agreement with experimental mass distributions for asymmetric fission modes. This improvement is found to be primarily due to the microscopic inertia tensor. To assess the effectiveness of the five-dimensional parametrization, the results are compared with those from lower-dimensional calculations. The Cassini parameter set $\{\alpha,\ \alpha_1,\ \alpha_3,\ \alpha_4,\ \alpha_6\}$ is shown to properly describe both mass asymmetry and superlong symmetric fission. Furthermore, a rare type of hot fission is observed for heavy fragment masses of 134 ± 2, characterized by a superelongated, neck-shaped light fragment.

DOI: 10.1103/dkjs-5fty

I. INTRODUCTION

Nuclear fission is the primary nuclear reaction in the actinide region. A notable characteristic of this phenomenon is the mass asymmetry observed in fission fragment mass distributions (FFMDs), which is particularly pronounced in the spontaneous and low-energy fission of light actinides. Experimental observations consistently demonstrate that asymmetric fission is the dominant mode, with heavy fragments predominantly clustering around mass number $A \approx 140$ [1,2]. This mass asymmetry presents a challenge to theoretical models, as simple shell-effect considerations would favor the formation of the doubly magic nuclei ^{132}Sn. This observation suggests the presence of a more complex structure of shell effects, with an additional asymmetric fission mode besides the one related to ^{132}Sn.

The mass asymmetry in the FFMDs of light actinide nuclei is often attributed to a combination of two asymmetric modes, Standard I and Standard II, along with the superlong symmetric fission mode [3,4]. Standard I and Standard II are associated with fragment masses near ^{132}Sn and $A \approx 140$, respectively. Recent studies employing superfluid dynamics [5] to determine nuclear density at scission point out that the shell effect responsible for Standard II is related to the nucleus ^{144}Ba with octupole deformation [6]. In the superheavy region, the inclusion of the octupole deformation produces a drastic change in the FFMD: from symmetric to asymmetric [7]. This highlights the importance of considering various fragment deformations for a comprehensive understanding of FFMDs, particularly the octupole.

Multidimensional Langevin equations have been extensively used to dynamically describe the fission process [8–14]. Fragment mass and total kinetic energy (TKE) derived from Langevin calculations are sensitive to physical quantities such as the deformation potential and the transport coefficients. For the deformation potential, quantitative calculation methods based on the macroscopic-microscopic method have become standard [15–17], and their physical interpretation is clear. In contrast, several approaches have been proposed for determining transport coefficients, ranging from macroscopic models based on hydrodynamic mass and one-body friction [18–20] to microscopic models derived from linear response theory of collective motion [21]. The effects of these transport coefficients on fission dynamics are less clear, especially in high-dimensional deformation spaces.

In the framework of the Langevin approach using three-quadratic-surface parametrization [22] or the two-center shell

*Contact author: okada.kazuki@jaea.go.jp

model (TCSM) [23], five-dimensional (5D) Langevin calculations with macroscopic transport coefficients have been achieved [13,24]. An innovative adaptation of the five-dimensional TCSM to near-barrier heavy-ion collisions was also proposed. For 4D calculations, both macroscopic and microscopic models have been utilized [11,12,14]. Discussions regarding the differences between macroscopic and microscopic transport coefficient approaches have been conducted within the 3D TCSM framework [25], and their impact on 3D Langevin calculations has been examined [10]. However, a consensus has not yet been reached. Therefore, further progress in this area requires verification through higher-dimensional calculations combined with a more flexible shape parametrization.

The Cassini shape parametrization offers an efficient description of nuclear shapes during fission [26]. In this parametrization, the deformed shapes of fissioning nuclei are described by a set of deformation parameters (α_n), used in a Legendre expansion of the original Cassini ovals, along with an overall elongation parameter (α). Within the framework of an improved scission point model which calculates FFMDs from the deformation potential by fixing α at the moment of neck rupture, the parameters α_1, α_3, α_4, and α_6 have been used in studies of both actinide [27,28] and superheavy nuclear regions [7,29]. For Langevin calculations of U and Fm fission, the relevance of each of these five parameters has also been assessed [30]. However, comprehensive 5D calculations incorporating all these parameters have not yet been performed. Moreover, investigations of high-dimensional calculations that use microscopic transport coefficients are needed to clarify their influence.

In this study, we investigate neutron-induced fission of ^{235}U using a 5D Langevin approach. The deformation coordinate space is defined by $\{\alpha, \alpha_1, \alpha_3, \alpha_4, \alpha_6\}$. We calculate the transport coefficients using both macroscopic and microscopic approaches to compare their respective influences on the fission process. The structure of this paper is as follows: Section II introduces the Cassini shape parametrization and the multidimensional Langevin equation as our methodology. Section III presents FFMDs and TKE distributions for thermal and 14 MeV neutron-induced fission. Section IV examines the dependence of fission on transport coefficients in thermal-neutron-induced fission. Section V compares the results from 5D calculations with those from lower-dimensional [three-dimensional (3D) and four-dimensional (4D)] calculations. Finally, Section VI concludes the paper.

II. NUMERICAL METHOD

A. Cassini shape parameterization

The nuclear shapes during the fission process are described using the Cassini oval parametrization [26], which is an effective method for representing the deformation of fissioning nuclei. The original Cassini ovals are defined as geometric figures, where $R =$ const in lemniscate coordinates (R, x). The transformation from lemniscate coordinates (R, x) to scaled cylindrical coordinates $(\bar{\rho}, \bar{z})$ is given by

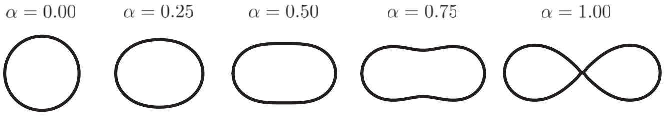

FIG. 1. Shapes of original Cassini ovals with $\alpha_n = 0$ for various values of α, illustrating the fission process.

$$\begin{aligned}
\bar{\rho} &= \frac{1}{\sqrt{2}}\sqrt{p(x) - R^2(2x^2-1) - s},\\
\bar{z} &= \frac{\text{sign}(x)}{\sqrt{2}}\sqrt{p(x) + R^2(2x^2-1) + s},\\
p(x) &\equiv \sqrt{R^4 + 2xR^2(2x^2-1) + s^2},\\
&-\infty \leqslant R \leqslant \infty, \quad 0 \leqslant x \leqslant 1.
\end{aligned} \tag{1}$$

Here, $s = \epsilon R_0^2$, where R_0 is the radius of a spherical nucleus and ϵ is the overall elongation parameter. The parameter ϵ describes the process of a single sphere evolving into two separate ovals. The regular cylindrical coordinates (ρ, z) are related to $(\bar{\rho}, \bar{z})$ by

$$\rho = \bar{\rho}/c, \quad z = (\bar{z} - \bar{z}_{\text{c.m.}})/c, \tag{2}$$

where the constants c and $\bar{z}_{\text{c.m.}}$ are determined by enforcing volume conservation and setting the center of mass at the origin of the (ρ, z) coordinate system, respectively.

To introduce a wider range of deformations, the Legendre expansion of R is employed:

$$R(x) = R_0\left[1 + \sum_n \alpha_n P_n(x)\right], \tag{3}$$

where $P_n(x)$ represents the nth Legendre polynomial. The deformed nuclear shapes are then characterized by the set of parameters α_n. However, using ϵ as elongation parameter leads to a significant dependence of the neck radius on α_n, which is not ideal for describing the last stage of the fission process. For this reason, instead of ϵ, an alternative elongation parameter α is defined as

$$\alpha \equiv \frac{\bar{z}_R^2 + \bar{z}_L^2 - 2\bar{\rho}^2(0)}{\bar{z}_R^2 + \bar{z}_L^2 + 2\bar{\rho}^2(0)}, \tag{4}$$

where $\bar{z}_R$ and $\bar{z}_L$ are the right and left endpoints of the Cassini oval on the z axis, and $\bar{\rho}(0)$ is the radius at $z = 0$. A direct relationship between ϵ and α can be derived from Eq. (4):

$$\begin{aligned}
\epsilon = \frac{\alpha - 1}{4}&\left[\left(1 + \sum_n \alpha_n\right)^2 + \left(1 + \sum_n (-1)^n \alpha_n\right)^2\right]\\
&+ \frac{\alpha + 1}{2}\left[1 + \sum_n (-1)^n \alpha_{2n}\frac{(2n-1)!!}{2^n n!}\right]^2.
\end{aligned} \tag{5}$$

Figure 1 illustrates representative shapes of generalized Cassini ovals for different values of α, with $\alpha_n = 0$. At $\alpha = 0$, the shape is spherical, and it elongates along the horizontal axis as α increases. A neck begins to form at the center of the Cassini oval when α exceeds approximately 0.5. At $\alpha = 1$,

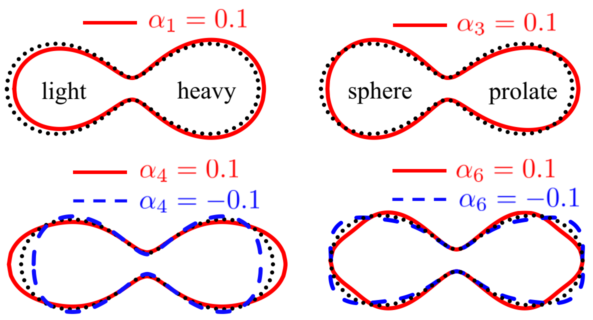

FIG. 2. Shape dependence of Cassini ovals on α_n at scission ($\alpha = 0.985$). The shape at $\alpha_n = 0$ is indicated by a black dotted line, and the shape at $\alpha_n = 0.1$ by a red solid line. For $n = 4$ and $n = 6$, shapes at $\alpha_n = -0.1$ (blue dotted line) are also shown.

this neck is zero. Thus, α serves as the primary fission coordinate. Furthermore, we define the scission line at $\alpha = 0.985$, where the neck radius is small but not zero, irrespective of the value of α_n.

For an efficient description of the fission process, the selection of appropriate deformation parameters is crucial. Notably, α_n parameters with odd n introduce asymmetric deformations, while those with even n introduce symmetric deformations. In this study, we employ a five-dimensional collective coordinate space $\{\alpha, \alpha_1, \alpha_3, \alpha_4, \alpha_6\}$. These coordinates correspond to: elongation (α), mass asymmetry (α_1), shape asymmetry (α_3), quadrupole deformation of fragments (α_4), and hexapole deformation of fragments (α_6). Figure 2 visually represents the deformations associated with each parameter. As can be seen, α_1 is essential for describing mass-asymmetric fission. α_3, another odd-n parameter, describes cases where one fragment is spherical while the other is elongated, thus playing a distinct role from α_1. α_4 is important not only at scission but also for describing symmetric deformations relevant to the ground state, the first barrier, and the second minimum. α_6 significantly influences the distance between the centers of mass of the fragments. Consequently, α_6 is expected to be critical for describing large symmetric deformations, such as those encountered in superlong or supershort symmetric fission modes.

B. Multidimensional Langevin equation

The five-dimensional Langevin equation is used to describe the fission process. In this approach, the deformation parameters $\{\alpha, \alpha_1, \alpha_3, \alpha_4, \alpha_6\}$ are the collective coordinates $\{q_i\}$ and the time evolution of $\{q_i\}$, and their conjugate momentum $\{p_i\}$ is described by

$$\begin{aligned}\frac{dq_i}{dt} &= m_{ij}^{-1} p_j,\\ \frac{dp_i}{dt} &= -\gamma_{ij} m_{jk}^{-1} p_k - \frac{\partial F}{\partial q_i} - \frac{1}{2}\frac{\partial m_{jk}^{-1}}{\partial q_i} p_j p_k + g_{ij} R_j, \end{aligned} \quad (6)$$

where m_{ij} is the inertia tensor and γ_{ij} is the friction tensor. Computational details for m_{ij} and γ_{ij} are provided in the subsequent subsection. F is the free energy calculated with the macroscopic-microscopic method [17] as the sum of the macroscopic potential and the microscopic correction as follows:

$$F(\boldsymbol{q}, T) = F_{\text{FRLDM}}(\boldsymbol{q}, T) + F_{\text{micro}}(\boldsymbol{q}, T), \quad (7)$$

with

$$F_{\text{FRLDM}}(\boldsymbol{q}, T) = V_{\text{FRLDM}}(\boldsymbol{q}) - a(\boldsymbol{q}) T^2. \quad (8)$$

Here, V_{FRLDM} is the finite-range liquid drop potential, and a is the level density parameter given in Ref. [31]. F_{micro} is the microscopic free energy calculated with the Strutinsky method [15,16], which takes into account the dependence of nuclear temperature T on the single-particle levels. Detailed calculation methods can be found in Refs. [21,32]. T is determined by the relation $E^* = aT^2$, with E^* being the excitation energy. E^* is calculated at each time step by the condition of energy conservation:

$$E^* = E_{\text{full}} - \tfrac{1}{2} m_{ij}^{-1} p_i p_j - F(\boldsymbol{q}, T = 0), \quad (9)$$

where E_{full} is the total energy of the system.

g_{ij} is determined by the Einstein relation $T^* \gamma_{ij} = g_{ik} g_{kj}$, where T^* is the effective nuclear temperature [33]. It is directly related to T by $T^* = (\hbar\omega/2)\coth(\hbar\omega/2T)$ where $\hbar\omega$ is the frequency of the collective motion. In this study, we use $\hbar\omega = 1.2$ MeV for all systems. The random number R_j is characterized by the white noise, with $\langle R_i(t)\rangle = 0$ and $\langle R_i(t) R_j(t')\rangle = 2\delta_{ij}\delta(t - t')$ where $\langle\rangle$ denotes the average over an ensemble.

C. Macroscopic and microscopic transport coefficients

In this study, two distinct approaches (macroscopic and microscopic) to determine transport coefficients are used. The macroscopic inertia tensor m_{ij}^{macro} is calculated with the Werner-Wheeler method [18], given as

$$m_{ij}^{\text{macro}} = \pi \rho_0 \int \rho^2(z)\left[A_i A_j + \frac{\rho^2(z)}{8}\frac{\partial A_i}{\partial z}\frac{\partial A_j}{\partial z}\right] dz, \quad (10)$$

with

$$A_i = \frac{1}{\rho^2}\frac{\partial}{\partial q_i}\int_{z_R}^{z} \rho^2(z') dz'. \quad (11)$$

The macroscopic friction tensor $\gamma_{ij}^{\text{macro}}$ is computed with the completed wall-and-window formula [19,20]. It is given by

$$\begin{aligned}\gamma_{ij}^{\text{macro}} &= k_s f(q)\gamma_{ij}^{\text{wall}} + (1 - f(q))\big(k_s \gamma_{ij}^{\text{wall2}} + \gamma_{ij}^{\text{window}}\big),\\ f(q) &= \sin^2\left(\frac{\pi}{2}\beta\right). \end{aligned} \quad (12)$$

Here, $\beta = \rho^2(0)/\rho_{\min}^2$, where $\rho_{\min}$ is the shorter semi-axis in the ρ direction of fragments. The magnitude of the friction tensor obtained using the wall formula is overestimated, and it is common practice to use k_s as a correction factor. In this study, we use $k_s = 0.25$ given in Ref. [34].

The dissipation based on the wall formula is expressed as

$$\gamma_{ij}^{\text{wall}} = \rho_0 v \int \frac{\partial \rho^2}{\partial q_i}\frac{\partial \rho^2}{\partial q_j}\left[4\rho^2 + \left(\frac{\partial \rho^2}{\partial z}\right)^2\right]^{-1/2} dz, \quad (13)$$

and

$$\gamma_{ij}^{\text{wall2}} = \rho_0 v\left(\int_{z_L}^{z_{\text{neck}}} I_L(z)dz + \int_{z_{\text{neck}}}^{z_R} I_R(z)dz\right), \tag{14}$$

with

$$I_{L,R}(z) = \left(\frac{\partial\rho^2}{\partial q_i} + \frac{\partial\rho^2}{\partial z}\frac{\partial z_{\text{c.m.}}^{L,R}}{\partial q_i}\right)\left(\frac{\partial\rho^2}{\partial q_j} + \frac{\partial\rho^2}{\partial z}\frac{\partial z_{\text{c.m.}}^{L,R}}{\partial q_j}\right) \times\left[4\rho^2 + \left(\frac{\partial\rho^2}{\partial z}\right)^2\right]^{-1/2}, \tag{15}$$

where $z_{\text{c.m.}}^L$ and $z_{\text{c.m.}}^R$ are the centers of mass of the left and right fragments. The additional term obtained from the window formula is

$$\gamma_{ij}^{\text{window}} = \frac{1}{2}\rho_0 v\left[\Delta\sigma\frac{\partial D_{\text{c.m.}}}{\partial q_i}\frac{\partial D_{\text{c.m.}}}{\partial q_j} + \frac{32}{9}\frac{1}{\Delta\sigma}\frac{\partial V_1}{\partial q_i}\frac{\partial V_1}{\partial q_j}\right],$$
$$\Delta\sigma = \pi\rho^2(0), \tag{16}$$

where $D_{\text{c.m.}}$ is the distance between $z_{\text{c.m.}}^L$ and $z_{\text{c.m.}}^R$, and V_1 is the volume of one fragment.

The microscopic transport coefficients are obtained by applying linear response theory to the collective motion of nuclei [21]. The inertia and the friction tensor are given by

$$\gamma_{ij}^{\text{micro}} = 2\hbar\sum_{\mu\nu}\left(n_\mu^T - n_\nu^T\right)\xi_{\nu\mu}^2\frac{E_{\nu\mu}^-\Gamma_{\nu\mu}}{\left[\left(E_{\nu\mu}^-\right)^2 + \Gamma_{\nu\mu}^2\right]^2}F_{\nu\mu}^i F_{\mu\nu}^j + 2\hbar\sum_{\mu\nu}\left(1 - n_\mu^T - n_\nu^T\right)\eta_{\nu\mu}^2\frac{E_{\nu\mu}^+\Gamma_{\nu\mu}}{\left[\left(E_{\nu\mu}^+\right)^2 + \Gamma_{\nu\mu}^2\right]^2}F_{\nu\mu}^i F_{\mu\nu}^j, \tag{17}$$

$$m_{ij}^{\text{micro}} = \hbar^2\sum_{\mu\nu}\left(n_\mu^T - n_\nu^T\right)\xi_{\nu\mu}^2\frac{E_{\nu\mu}^-\left[\left(E_{\nu\mu}^-\right)^2 - 3\Gamma_{\nu\mu}^2\right]}{\left[\left(E_{\nu\mu}^-\right)^2 + \Gamma_{\nu\mu}^2\right]^2}F_{\nu\mu}^i F_{\mu\nu}^j + \hbar^2\sum_{\mu\nu}\left(1 - n_\mu^T - n_\nu^T\right)\eta_{\nu\mu}^2 \times\frac{E_{\nu\mu}^+\left[\left(E_{\nu\mu}^+\right)^2 - 3\Gamma_{\nu\mu}^2\right]}{\left[\left(E_{\nu\mu}^+\right)^2 + \Gamma_{\nu\mu}^2\right]^2}F_{\nu\mu}^i F_{\mu\nu}^j. \tag{18}$$

Here E_ν is the quasi-particle energy, $n_\nu^T \equiv [1 + \exp(E_\nu/T)]^{-1}$, $E_{\nu\mu}^\pm = E_\nu \pm E_\mu$, $\eta_{\nu\mu} = u_\nu v_\mu + u_\mu v_\nu$, $\xi_{\nu\mu} = u_\nu u_\mu - v_\mu v_\nu$, where u_ν and v_ν are the coefficients of the Bogoliubov-Valatin transformation. The effects of the mean-field Hamiltonian are included as a single-particle operator $F_{\mu\nu}^i$, reflecting quantum effects such as the shell effects in the transport coefficients. Moreover, a key distinction between microscopic and macroscopic transport coefficients is that the former inherently depends on temperature T.

To illustrate the differences between the two types of coefficients, the diagonal components of the tensors are examined. Figure 3 shows the ratio of the microscopic to the macroscopic transport coefficients, $m_{11}^{\text{micro}}/m_{11}^{\text{macro}}$ and $\gamma_{11}^{\text{micro}}/\gamma_{11}^{\text{macro}}$, along α at $T = 0.0$, 0.5, 1.0, 1.5, 2.0 MeV. Here, the subscript "1" denotes α. The fine oscillations observed in the figure are attributed to quantum effects arising from microscopic calculations. The friction tensor is seen to increase with temperature, whereas the inertia tensor decreases. At lower temperatures, the macroscopic friction coefficient exhibits larger values, while above approximately 0.5 MeV, the microscopic friction becomes larger. The timescale in fission dynamics is generally determined by the transport coefficients; such subtle structures and temperature dependencies are expected to have a significant impact on the fission process.

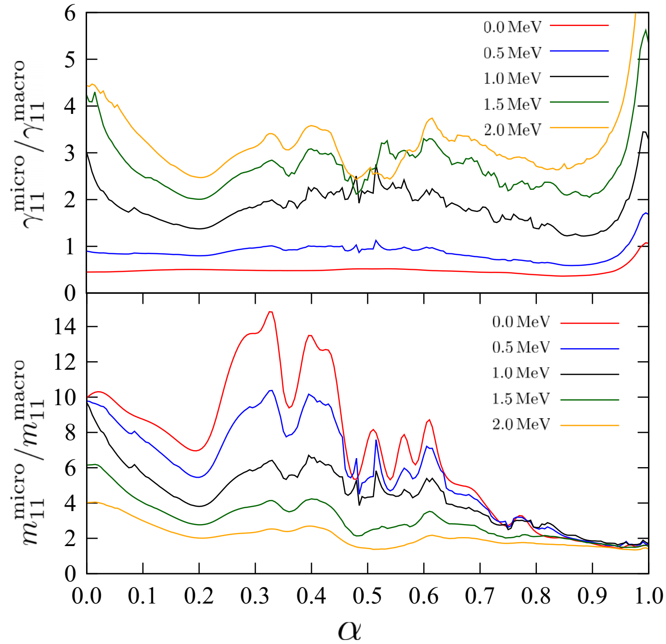

FIG. 3. Temperature dependence of the microscopic transport coefficients along α at $\alpha_n = 0$. The $\alpha\alpha$ components are plotted as ratios to macroscopic transport coefficients for several temperatures T. The top panel shows the friction tensor, while the bottom panel shows the inertia tensor.

For the investigation of fission dynamics at low excitation energies, such as thermal-neutron-induced fission, the transport coefficients near the second barrier ($\alpha = 0.65$) are shown, at $T = 0$, as a function of the mass asymmetry α_1 in Fig. 4. The diagonal components of the transport coefficients are presented for the deformation coordinates $\{\alpha, \alpha_1, \alpha_3, \alpha_4, \alpha_6\}$. It is found that the microscopic friction tensor has approximately half the value of macroscopic ones, except for γ_{22}, the $\alpha_1\alpha_1$ component. The component γ_{22} is clearly reduced in the symmetric fission region, suggesting that the use of microscopic friction coefficients facilitates changes in the mass numbers of fragments. The microscopic inertia tensor exhibits values that are approximately ten times larger than those of the macroscopic tensor. However, it should be noted that the components m_{22} and m_{33}, which are strongly related to asymmetry, show significant decreases near $\alpha_1 = \pm 0.1$. In regions with strong asymmetry, the smaller inertia tensor is expected to guide the Brownian particle in that direction.

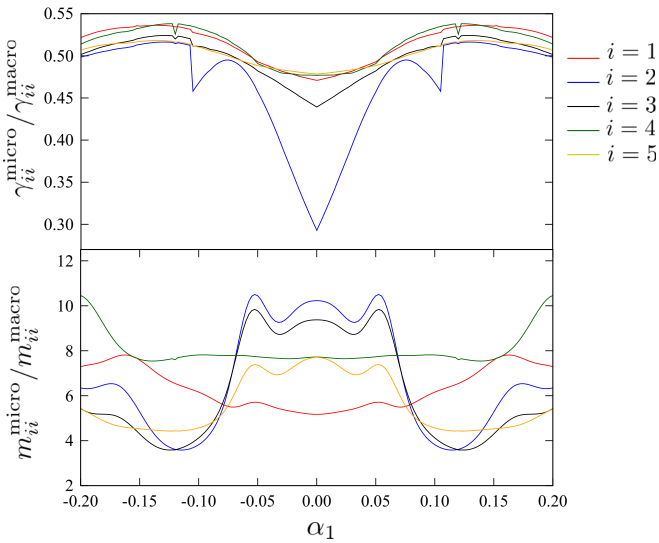

FIG. 4. Diagonal components of the microscopic transport coefficients as a function of α_1 at $\alpha = 0.65$ and $T = 0$. Five components are shown: $\alpha, \alpha_1, \alpha_3, \alpha_4$ and α_6. The upper panel shows the friction tensor, while the bottom panel shows the inertia tensor.

III. RESULTS

A. Fragment mass and TKE distributions for neutron-induced fission of ^{235}U

As a representative case in the actinide region, we examine the neutron-induced fission of ^{235}U at both thermal and 14 MeV incident neutron energies. For the transport coefficients, both patterns are used: microscopic (m_{ij}^{micro}, $\gamma_{ij}^{\mathrm{micro}}$) and macroscopic ($m_{ij}^{\mathrm{macro}}$, $\gamma_{ij}^{\mathrm{macro}}$) transport coefficients. For all calculations, we performed at least 100 000 fission events to obtain fragment distributions.

Figure 5 presents the resulting FFMDs of ^{236}U. All results indicate the dominance of asymmetric fission. In the case of thermal-neutron-induced fission, the distribution obtained using microscopic transport coefficients shows a peak at $A_H = 138$, which is in better agreement with experimental data compared with the peak at $A_H = 136$ obtained using macroscopic ones. One can consider that the microscopic transport coefficients, which incorporate shell effects and their temperature dependence, provide a more accurate description of the mass asymmetry. On the other hand, for the 14 MeV neutron-induced fission, the calculated FFMDs show little dependence on the choice of transport coefficients.

Figure 6 presents the two-dimensional distributions of fragment mass and TKE. In all cases, the asymmetric fission mode and the superlong symmetric fission mode, which is characterized by low TKE, are shown. The yield of the superlong symmetric fission mode is found to increase with increasing incident neutron energy. A broad TKE distribution for each fragment mass is observed across both incident neutron energies, which is evident in relation to the black line representing the average TKE. The average TKE for each mass number of the heavy fragment in thermal-neutron-induced fission is also shown in Fig. 7. The high TKE near $A_H = 132$ can be reproduced using macroscopic transport

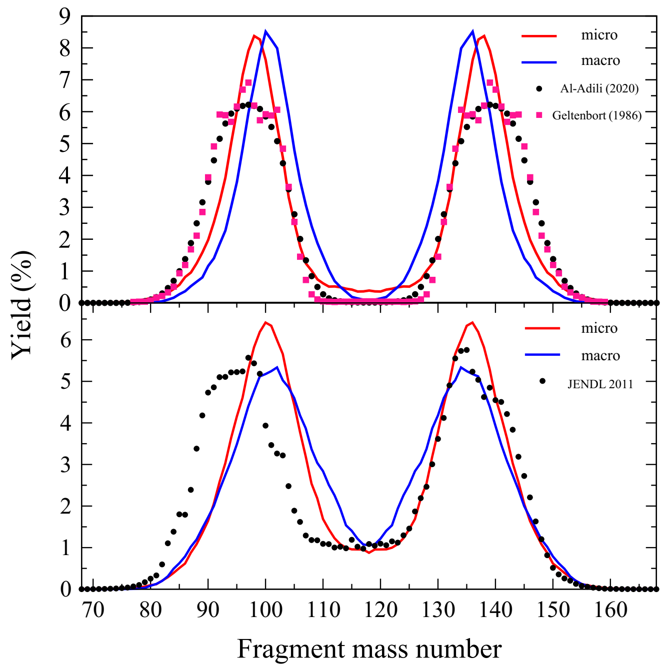

FIG. 5. FFMDs for thermal (top) and 14 MeV (bottom) neutron-induced fission of ^{235}U calculated using the macroscopic (blue squares) and the microscopic (red circles) transport coefficients. The experimental data are given in Refs. [35] and [2] for thermal-neutron-induced fission and in Ref. [36] for 14 MeV neutron-induced fission.

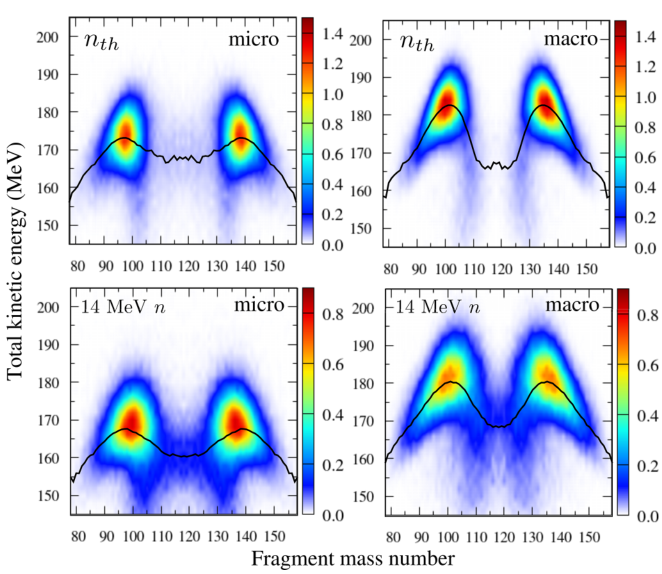

FIG. 6. Fragment mass and TKE distributions for the neutron-induced fission of ^{235}U. The left panels show the results calculated with the microscopic transport coefficients and the right panels show those calculated with macroscopic ones. The upper panels give the system with thermal-neutron-induced fission, while the bottom panels give those with the 14 MeV neutron-induced fission. The color bar represents the yield within $\Delta A = 1$ and $\Delta\mathrm{TKE} = 2$ MeV. The black line shows the average values of TKE plotted as a function of fragment mass number.

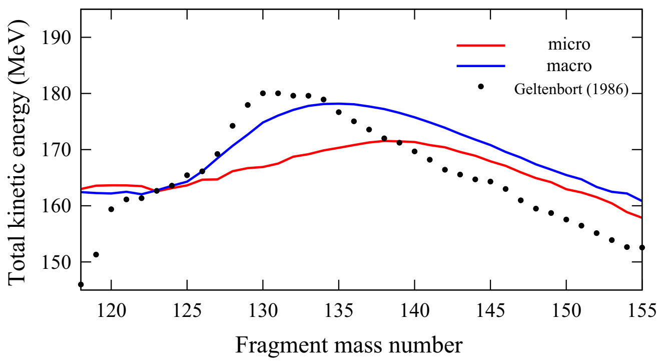

FIG. 7. Average TKE as a function of heavy-fragment mass for thermal-neutron-induced fission of ^{235}U. The experimental data are taken from Ref. [2].

coefficients; however, TKE is overestimated for heavier mass numbers. When microscopic transport coefficients are used, TKE is overestimated specifically in the region of symmetric separation, and the distribution has a peak around $A_H = 140$.

Striking in Fig. 6 are the long (low-energy) tails of the TKE distributions around the complementary masses (102,134). They are present in all cases. They could represent a distinct mode of fission with extremely elongated and/or slowly moving fragments at scission. To separate these two possible causes, we replace, in Fig. 8, the TKE with the kinetic energy at the moment of neck rupture (KEpre).

Since the prescission kinetic energies do not show tails to the low-energy side, the tail seen in Fig. 6 may be attributable to tails in the TKE caused by the Coulomb repulsion, namely, a very large elongation corresponding to a large $D_{\text{c.m.}}$, which is the distance between the centers of mass of two nascent fragments at scission. This is confirmed in Fig. 9, where the same fission events are represented in the $(A_F, D_{\text{c.m.}})$ plane. As expected, tails appear at large $D_{\text{c.m.}}$ values (as large as $3.1R_0$, $R_0 = 1.28A^{1/3}$) around the fragment masses 102 and 134.

As a consequence, we could anticipate the presence of a low-energy tail in the experimental TKE distribution since, according to our estimate, this type of fission represents 4% of the total yield, hence non-negligible. Figure 10 compares the

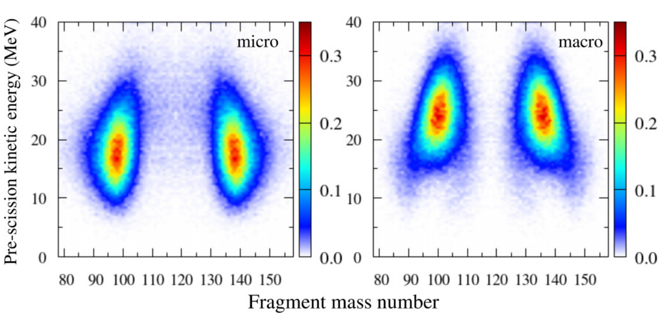

FIG. 8. Fragment mass and prescission kinetic energy distributions for the neutron-induced fission of ^{235}U. The left panel shows the result calculated with the microscopic transport coefficients, and the right panel shows that calculated with macroscopic ones. The color bar represents the yield within $\Delta A = 1$ and $\Delta\text{KEpre} = 2$ MeV.

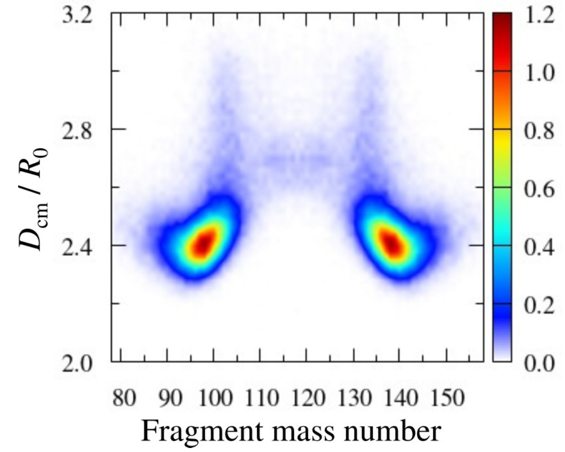

FIG. 9. Distributions of fragment mass and distance between the centers of mass of the fragments for the thermal-neutron-induced fission of ^{235}U, calculated with the microscopic transport coefficients. The color bar represents the yield within $\Delta A = 1$ and $\Delta D_{\text{c.m.}} = 0.2R_0$.

calculated TKE distribution with data from Ref. [37]. We see that the calculations agree very well with the most probable value measured, underestimate the width, and show a tail at low energies which is not present in the data. This is not surprising since our calculated value (Coulomb repulsion plus prescission kinetic energy) represents the TKE that will be measured if nothing else happens after scission.

In reality, the division into mass ratio 134/102 is a special type of fission with a unique series of more and more deformed light fragments, as seen in Fig. 11. At the limit, in these fragments, a second neck appears. These very elongated fragments cannot survive as such to reach the detector. They will either split again into two fragments or emit a large number (at least five) of neutrons. Both outcomes will modify the TKE as compared with what we predicted when we stopped the calculations at scission. A ternary event, for instance, will have a larger TKE reducing the initial tail and even producing the opposite effect. The TKE distribution is therefore not the ideal observable to prove the existence of a very elongated light fragment at scission. A dedicated experiment looking for three fragments or for an excessive number of prompt

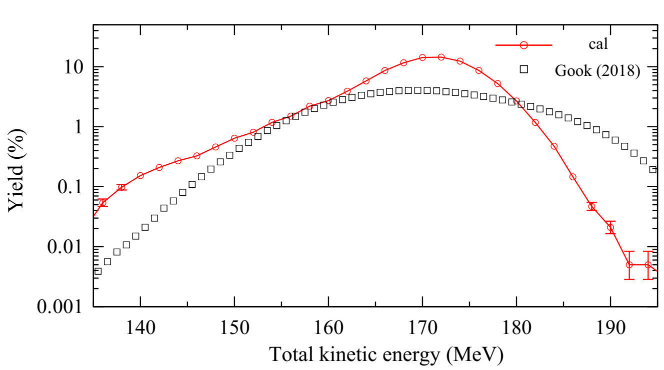

FIG. 10. Fragment TKE distribution for the neutron-induced fission of ^{235}U. The experimental data are taken from Ref. [37].

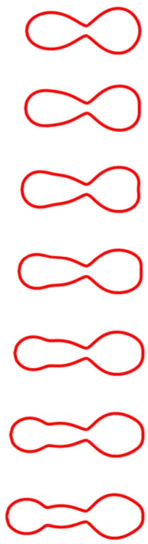

D_{cm}	$\langle\alpha\rangle$	$\langle\alpha_1\rangle$	$\langle\alpha_3\rangle$	$\langle\alpha_4\rangle$	$\langle\alpha_6\rangle$
$2.4R_0$	0.985	-0.003	-0.120	0.010	0.014
$2.5R_0$	0.985	-0.026	-0.172	0.019	-0.021
$2.6R_0$	0.985	-0.049	-0.236	0.048	-0.048
$2.7R_0$	0.985	-0.038	-0.235	0.108	-0.056
$2.8R_0$	0.985	-0.038	-0.269	0.178	-0.053
$2.9R_0$	0.985	-0.047	-0.339	0.240	-0.066
$3.0R_0$	0.985	-0.050	-0.407	0.318	-0.075

FIG. 11. Average scission shapes along the tails calculated for the range $A_H = 132$ to 136, with their corresponding deformation parameters. All shapes show the light fragment on the left side and the heavy fragment on the right side.

neutrons is necessary. Additional postscission calculations are also necessary to help design such an experiment. In ^{252}Cf (sf), both outcomes (three fragments [38] and a very hot fission mode only for one mass ratio, 144/106 [39]) have been observed. So we cannot exclude similar processes during ^{235}U (n_{th}, f).

In the present study, the low TKE tail present at fragment mass ratios around 134/102 is theoretically predicted. The scission shapes corresponding to these very low TKE are not unusual. They are typical scission shapes in very heavy and superheavy nuclei. See Fig. 2 in Ref. [7] and Fig. 2 in Ref. [29].

Coming back to Fig. 8, one can see that the difference between "micro" and "macro" TKE is mainly due to KEpre; it is an indication that the "micro" dynamics between saddle and scission is more dissipative.

B. Influence of transport coefficients on fission dynamics

To analyze the influence of the transport coefficients on fission dynamics in more detail, we conduct a systematic investigation. The transport coefficients consist of inertia and friction; in the previous section, either the macroscopic approach or the microscopic approach is used consistently for both components. This is the standard way. In this chapter, we examine the properties of inertia and friction across four patterns using combinations of macroscopic and microscopic tensors. We focus only on thermal-neutron-induced fission since the distinction between macroscopic and microscopic approaches becomes less pronounced at high temperatures. For clarity in this discussion, we write the inertia and friction tensors without subscripts, simply as m and γ, respectively. Additionally, we denote macroscopic as "M" and microscopic

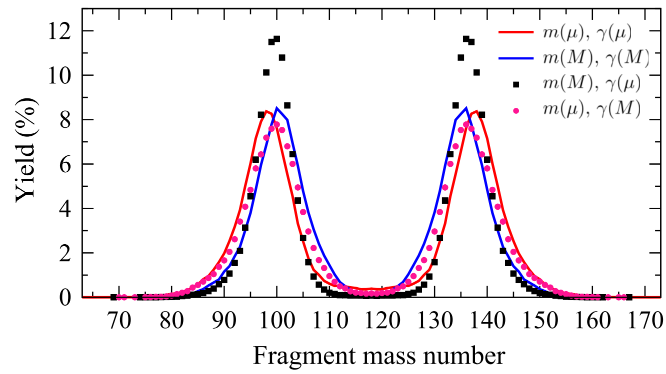

FIG. 12. FFMDs for the thermal-neutron-induced fission of ^{235}U. The blue and red solid lines represent the same data as Fig. 5. The black squares show FFMDs using the combination of $m(M)$ and $\gamma(\mu)$, while the pink circles represent those using $m(\mu)$ and $\gamma(M)$.

as "μ." For instance, the inertia tensor calculated using the microscopic approach is expressed as $m(\mu)$.

Figure 12 shows the FFMD results for all four patterns. When using $\{m(\mu), \gamma(M)\}$, the distribution shows an average value intermediate between $\{m(\mu), \gamma(\mu)\}$ and $\{m(M), \gamma(M)\}$ results, with no significant change in the width. However, the combination of $\{m(M), \gamma(\mu)\}$ shows the distribution concentrated in a narrower mass region with notably high peaks. This indicates that the choice of transport coefficients significantly affects FFMDs, particularly showing that the inertia tensor substantially influences peak height and distribution width. Furthermore, it should be emphasized that only when using the microscopic approach for both inertia and friction does the distribution show peak positions at the outermost regions, indicating the presence of Standard II.

The evolution of FFMDs during the process from the region before the second saddle point to the scission is considered to play a crucial role in evaluating the effects of transport coefficients. Figure 13 illustrates the differences between the $\{m(\mu), \gamma(\mu)\}$ distribution and the three other distributions along α. Just after passing the second barrier, all patterns show similar distributions. As the system approaches scission, distributions using $\{m(\mu), \gamma(\mu)\}$ demonstrate an increased yield in regions corresponding to Standard II, while other cases show higher yields in Standard I regions. Notably, when employing $\{m(M), \gamma(\mu)\}$, the distribution changes significantly even in the prescission region ($\alpha > 0.85$). This suggests that when both transport coefficients are small, particles experiencing Brownian motion become more susceptible to potential energy landscape variations, resulting in considerable changes in fragment shape even shortly before scission. However, this outcome is generally considered less physically realistic. In conclusion, $\{m(\mu), \gamma(\mu)\}$ configuration provides the most physically plausible FFMDs.

Figures 14 and 15 show the two-dimensional distributions of fragment mass versus quadrupole deformation β_2 and octupole deformation β_3 in thermal-neutron-induced ^{235}U fission. In the asymmetric fission region, while the deformation of heavy fragments is concentrated in a narrow range, the light fragments are found to show a broader distribution of

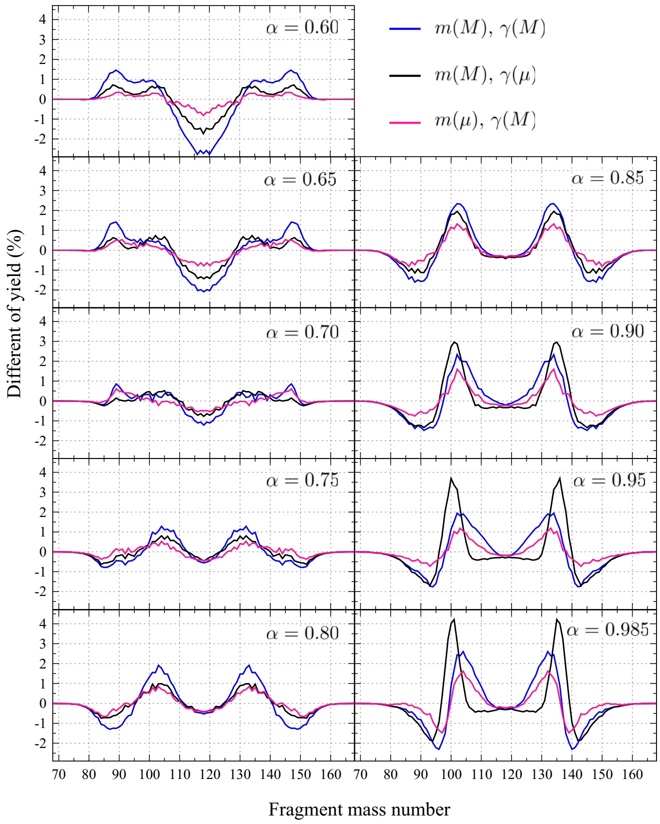

FIG. 13. Difference between the FFMDs for $\{m(\mu), \gamma(\mu)\}$ case and other distributions along the fission path from $\alpha = 0.6$ to $\alpha = 0.985$. The blue line shows the result with $\{m(\mu), \gamma(\mu)\}$, the black line shows that with $\{m(M), \gamma(\mu)\}$, and the pink line shows that with $\{m(\mu), \gamma(M)\}$.

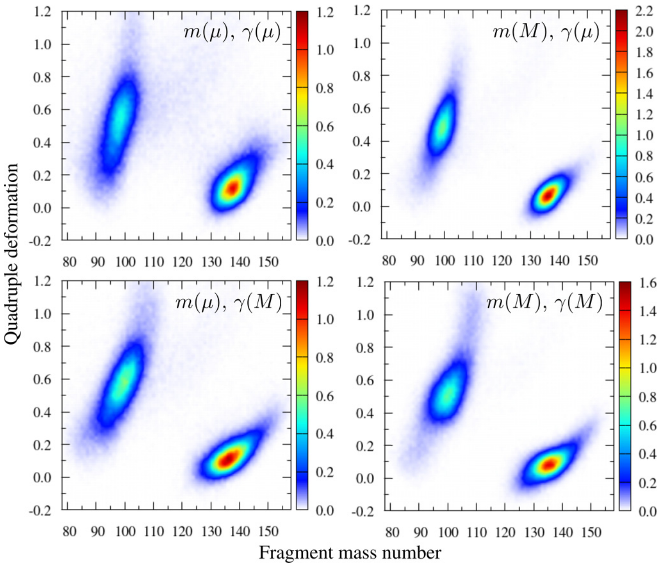

FIG. 14. Two-dimensional plots of distributions for the thermal-neutron-induced fission of ^{235}U in the (fragment mass, β_2) plane. The panels show the results calculated with the four combinations of microscopic and macroscopic transport coefficients mentioned in the text.

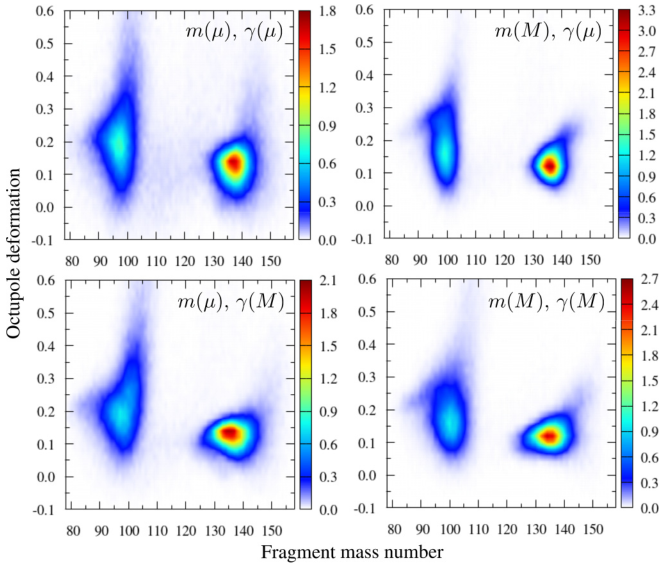

FIG. 15. Same as in Fig. 14, but the horizontal axis is changed to the fragment β_3.

deformation. Since the heavy fragment distribution is characterized by a unimodal structure, it is difficult to clearly distinguish between the Standard I and Standard II modes. However, it is observed that different combinations of transport coefficients affect the distribution patterns near the Standard I and II modes.

The validity of the distributions shown in Figs. 14 and 15 is assessed by comparing them with the average neutron multiplicity as a function of fragment mass presented in Fig. 5 of Ref. [40]. This distribution displays a sawtooth structure, where the multiplicity is high in the light fragment region, decreases with increasing mass, and then increases again. Focusing on heavy fragments, it has a minimum value around $A_H = 132$, indicating that fragments corresponding to this mass have small deformation. From Figs. 14 and 15, the values of β_2 and β_3 are small near $A_H = 132$, and they increase for heavier masses, confirming consistency with the observed average neutron multiplicity.

In Figs. 16 and 17, detailed structural analysis is performed by selecting distributions corresponding to narrow windows around $A_H = 132$ and 144. Figure 16 shows that the peak positions of the distributions are shifted in the two asymmetric modes. Specifically, at $A_H = 132$, heavy fragments are found to exhibit near-spherical shapes, while at $A_H = 144$, significant deformation is observed. Moreover, results from $m(\mu)$ and $\gamma(\mu)$ show broad distributions, indicating events with diverse deformations. It is noted that the proportion of $A_H = 144$ is small in FFMDs. When $m(\mu)$ is used, many events are distributed in the broad regions, and the resulting peaks of FFMDs are located in the outer regions. To obtain results consistent with experimental data, calculations using $m(\mu)$ should show peaks at even larger β_3 values, but this limitation is likely attributed to the current shape parametrization. Additionally, it is concluded that the type of friction consistently has minimal impact.

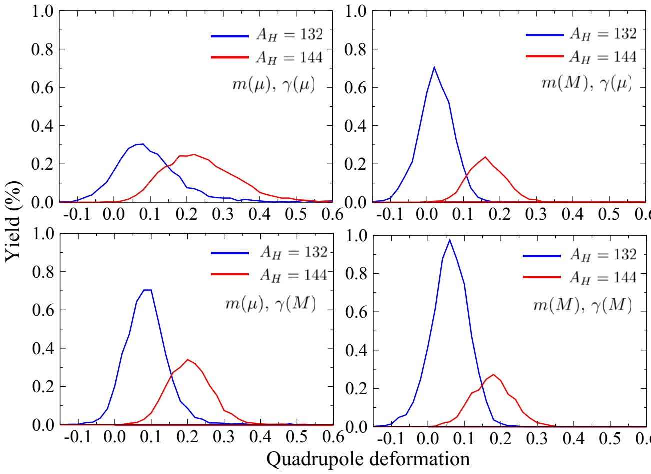

FIG. 16. Projections of the distributions in Fig. 14 at $A_H = 144$ (red line) and $A_H = 132$ (blue line). Four patterns are shown: $\{m(\mu), \gamma(\mu)\}$ (top left), $\{m(M), \gamma(\mu)\}$ (top right), $\{m(\mu), \gamma(M)\}$ (bottom left), and $\{m(M), \gamma(M)\}$ (bottom right).

C. Comparison of fragment mass and TKE distributions from three-, four- and five-dimensional Langevin calculations

To demonstrate the validity of the 5D Cassini parameter space $\{\alpha, \alpha_1, \alpha_3, \alpha_4, \alpha_6\}$, we compare the 5D results with the 3D $\{\alpha, \alpha_1, \alpha_4\}$ and 4D $\{\alpha, \alpha_1, \alpha_3, \alpha_4\}$ results, examining the fragment mass and kinetic energy distributions. In all calculations, the microscopic transport coefficients are used.

Figure 18 shows the results. Comparing 3D and 4D calculations, one can see that the addition of α_3 gives a significant shift of the mass distribution peak towards the inner region, showing that α_3 is important. When α_6 is added, extending to 5D, only the height of the peak around the symmetric division changes. This is because α_6 is a deformation parameter related to symmetric deformations. Furthermore, for 14 MeV neutron-induced fission, there is almost no difference between the results using 4D and 5D calculations.

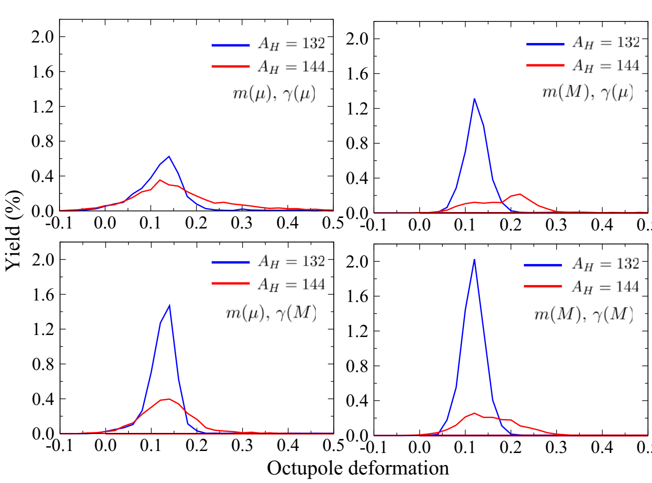

FIG. 17. The same as in Fig. 16, but the vertical axis is changed to the fragment β_3.

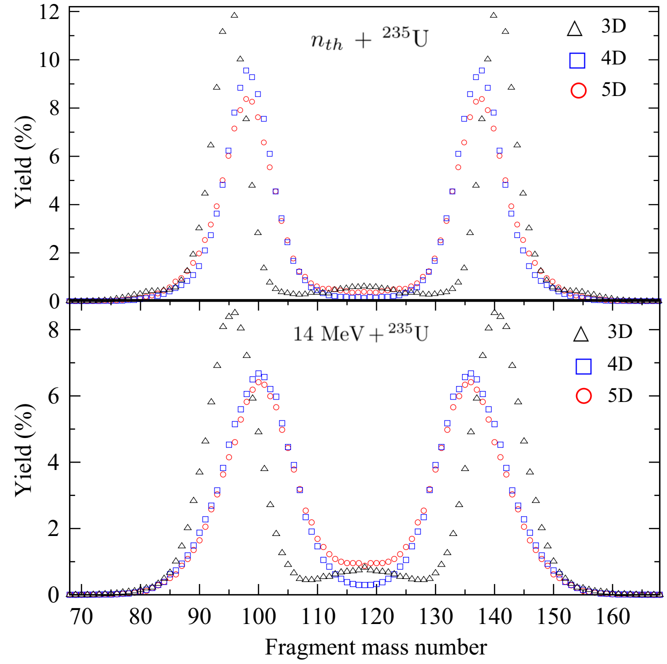

FIG. 18. Fragment mass distributions for thermal (upper) and 14 MeV (lower) neutron-induced fission of ^{235}U calculated with the 3D $\{\alpha, \alpha_1, \alpha_4\}$, 4D $\{\alpha, \alpha_1, \alpha_3, \alpha_4\}$, and 5D Langevin equations.

To further investigate the influence of α_6, we focus on the mass-TKE distributions. Figure 19 shows the distribution of total kinetic energy and fragment mass number for the fission of ^{236}U. The left panels depict the results for the 3D

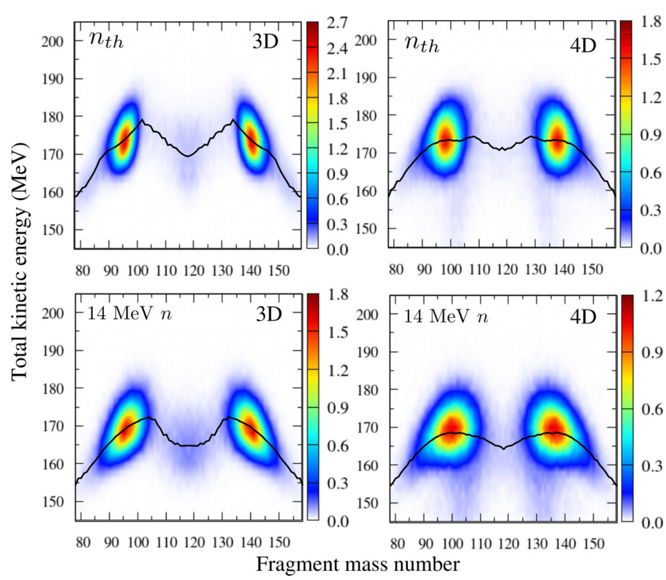

FIG. 19. Fragment mass and TKE distributions calculated with 3D and 4D Langevin equations. The left panels show the result calculated with thermal-neutron-induced fission, while the right panels give that with the 14 MeV neutron-induced fission. The black line shows the average values of TKE plotted as a function of fragment mass number.

case $\{\alpha, \alpha_1, \alpha_4\}$, while the right panels show the 4D case $\{\alpha, \alpha_1, \alpha_3, \alpha_4\}$. The solid lines in the plots represent the mean values of the distributions for each mass number. There is no significant difference in the asymmetric fission region distributions. However, near the symmetric fission mass number of 118, the mean kinetic energy of the fission fragments is lower in the 5D cases as shown in Fig. 6. This reduction in Coulomb energy is attributed to the fact that including α_6 allows for the description of the superlong symmetric fission mode. This effect is particularly pronounced in the case of 14 MeV neutron-induced fission, where the TKE decreases significantly despite no change in the FFMD.

As a conclusion, α_6 is effective in explaining the low total kinetic energy in the symmetric fission of nuclei such as ^{236}U and plays an important role in describing the superlong shape of fissioning nuclei. This 5D Cassini parameter set can flexibly represent not only mass asymmetry but also the overall fragment deformation related to TKE. It is expected to be effective also in the description of supershort symmetric fission observed in neutron-rich nuclei in the heavier actinide region [4].

IV. SUMMARY

In this study, we investigated the effects of transport coefficients and dimensionality of deformation space on fission dynamics in neutron-induced fission of ^{235}U by solving the five-dimensional Langevin equation in $\{\alpha, \alpha_1, \alpha_3, \alpha_4, \alpha_6\}$ space. We applied and compared both macroscopic and microscopic models for transport coefficients.

The results showed that microscopic transport coefficients incorporating shell effects and their temperature dependence improved the description of fission fragment mass distributions, particularly in thermal-neutron-induced fission, compared to macroscopic transport coefficients. By the application of microscopic models to both the inertia and friction tensors, wide distributions of the fragments β_2 and β_3 are obtained, allowing diverse deformations to be achieved by heavy fragments. In particular, it is found that the microscopic inertia tensor significantly contributes to improved reproducibility of mass distribution in thermal-neutron-induced fission of ^{235}U. Additionally, microscopic transport coefficients predicted broader fragment deformation distributions, especially for heavy fragments, suggesting the existence of more diverse fission pathways.

Comparison of three-, four-, and five-dimensional Langevin calculations revealed that the inclusion of the α_3 parameter (shape asymmetry) in four-dimensional calculations significantly improved agreement with experimental data. Furthermore, incorporating the α_6 parameter (related to nuclear elongation at fission) in five-dimensional calculations enabled the description of superlong symmetric fission modes. This mode is characterized by low total kinetic energy (TKE) in the region of symmetric separation and is particularly visible in two-dimensional mass-TKE distributions.

A rare type of hot fission, located around $A_H = 134$, with a very elongated, neck-shaped light fragment was observed. It may lead to sequential ternary fission or to fission events accompanied by more than five neutrons. This possibility should definitely be explored.

In conclusion, this study demonstrated the importance of considering microscopic transport coefficients and five-dimensional deformation space in the Langevin approach. The combination of five-dimensional Cassini shape parametrization and microscopic transport coefficients provides a powerful framework for understanding complex fission fragment properties such as mass asymmetry, fragment deformation, and TKE distribution.

In the future, the present approach will be applied to other actinide nuclei and validated across a broader range of excitation energies and fissioning systems.

ACKNOWLEDGMENTS

This work was supported by Grant-in-Aid for Research Activity Start-up (KAKENHI), Grant No. JP24K22887. Numerical computations in this study were performed at the Yukawa Institute Computer Facility and the Cybermedia Center.

DATA AVAILABILITY

Data are available within the article. Data are not publicly available upon publication because it is not technically feasible and/or the cost of preparing, depositing, and hosting the data would be prohibitive within the terms of this research project. Data are not publicly available. The data are available from the authors upon reasonable request.

[1] K. H. Schmidt, S. Steinhäuser, C. Böckstiegel, A. Grewe, A. Heinz, A. R. Junghans, J. Benlliure, H. G. Clerc, M. de Jong, J. Müller, M. Pfützner, and B. Voss, Nucl. Phys. A **665**, 221 (2000).
[2] P. Geltenbort, F. Gönnenwein, and A. Oed, Radiat. Eff. **93**, 57 (1986).
[3] F. Hambsch, H. Knitter, C. Budtz-Jørgensen, and J. Theobald, Nucl. Phys. A **491**, 56 (1989).
[4] U. Brosa, S. Grossmann, and A. Müller, Phys. Rep. **197**, 167 (1990).
[5] G. Scamps, C. Simenel, and D. Lacroix, Phys. Rev. C **92**, 011602(R) (2015).
[6] G. Scamps and C. Simenel, Nature (London) **564**, 382 (2018).
[7] N. Carjan, F. Ivanyuk, and Y. Oganessian, Nucl. Phys. A **968**, 453 (2017).
[8] T. Wada, Y. Abe, and N. Carjan, Phys. Rev. Lett. **70**, 3538 (1993).
[9] Y. Aritomo and S. Chiba, Phys. Rev. C **88**, 044614 (2013).
[10] M. D. Usang, F. A. Ivanyuk, C. Ishizuka, and S. Chiba, Phys. Rev. C **94**, 044602 (2016).

[11] M. D. Usang, F. A. Ivanyuk, C. Ishizuka, and S. Chiba, Phys. Rev. C **96**, 064617 (2017).
[12] C. Ishizuka, M. D. Usang, F. A. Ivanyuk, J. A. Maruhn, K. Nishio, and S. Chiba, Phys. Rev. C **96**, 064616 (2017).
[13] A. J. Sierk, Phys. Rev. C **96**, 034603 (2017).
[14] K. Shimada, C. Ishizuka, F. A. Ivanyuk, and S. Chiba, Phys. Rev. C **104**, 054609 (2021).
[15] V. M. Strutinsky, Nucl. Phys. A **95**, 420 (1967).
[16] V. M. Strutinsky, Nucl. Phys. A **122**, 1 (1968).
[17] P. Möller, A. J. Sierk, T. Ichikawa, and H. Sagawa, At. Data Nucl. Data Tables **109-110**, 1 (2016).
[18] K. Davies, A. Sierk, and J. Nix, Phys. Rev. C **13**, 2385 (1976).
[19] J. Blocki, Y. Boneh, J. R. Nix, J. Randrup, M. Robel, A. J. Sierk, and W. J. Swiatecki, Ann. Phys. **113**, 330 (1978).
[20] J. Randrup and W. Swiatecki, Nucl. Phys. A **429**, 105 (1984).
[21] F. Ivanyuk and H. Hofmann, Nucl. Phys. A **657**, 19 (1999).
[22] J. Rayford Nix, Nucl. Phys. A **130**, 241 (1969).
[23] J. Maruhn and W. Greiner, Z. Phys. **251**, 431 (1972).
[24] F. A. Ivanyuk, C. Ishizuka, and S. Chiba, Phys. Rev. C **109**, 034602 (2024).
[25] F. Ivanyuk, S. Chiba, and Y. Aritomo, Nucl. Sci. Tech. **53**, 737 (2016).
[26] V. V. Pashkevich, Nucl. Phys. A **169**, 275 (1971).
[27] N. Carjan, F. Ivanyuk, Y. Oganessian, and G. Ter-Akopian, Nucl. Phys. A **942**, 97 (2015).
[28] N. Carjan, F. A. Ivanyuk, and Y. T. Oganessian, J. Phys.: Conf. Ser. **863**, 012044 (2017).
[29] N. Carjan, F. A. Ivanyuk, and Y. T. Oganessian, Phys. Rev. C **99**, 064606 (2019).
[30] K. Okada, T. Wada, and N. Carjan, EPJ Web Conf. **284**, 04018 (2023).
[31] J. Tōke and W. Światecki, Nucl. Phys. A **372**, 141 (1981).
[32] F. A. Ivanyuk, C. Ishizuka, M. D. Usang, and S. Chiba, Phys. Rev. C **97**, 054331 (2018).
[33] H. Hofmann, C. Grégoire, R. Lucas, and C. Ngô, Z. Phys. A **293**, 229 (1979).
[34] A. V. Karpov, P. N. Nadtochy, D. V. Vanin, and G. D. Adeev, Phys. Rev. C **63**, 054610 (2001).
[35] A. Al-Adili, D. Tarrío, K. Jansson, V. Rakopoulos, A. Solders, S. Pomp, A. Göök, F.-J. Hambsch, S. Oberstedt, and M. Vidali, Phys. Rev. C **102**, 064610 (2020).
[36] K. Shibata, O. Iwamoto, T. Nakagawa, N. Iwamoto, A. Ichihara, S. Kunieda, S. Chiba, K. Furutaka, N. Otuka, T. Ohsawa, *et al.*, J. Nucl. Sci. Technol. **48**, 1 (2011).
[37] A. Göök, F.-J. Hambsch, S. Oberstedt, and M. Vidali, Phys. Rev. C **98**, 044615 (2018).
[38] Y. V. Pyatkov, D. Kamanin, N. Carjan, K. Okada, Z. Goryainova, E. Kuznetsova, V. Malaza, A. Strekalovsky, O. Strekalovsky, S. Wyngaardt, *et al.*, J. Phys.: Conf. Ser. **2586**, 012038 (2023).
[39] S.-C. Wu, R. Donangelo, J. O. Rasmussen, A. V. Daniel, J. K. Hwang, A. V. Ramayya, and J. H. Hamilton, Phys. Rev. C **62**, 041601(R) (2000).
[40] K. Nishio, Y. Nakagome, H. Yamamoto, and I. Kimura, Nucl. Phys. A **632**, 540 (1998).